Supporting Information

Reversible single crystal photochemistry and spin state switching in a metal-cyanide complex

Michał Magott, Mirosław Arczyński, Leszek Malec, Michał Rams, Mathieu Rouzières, Andrei Rogalev, Fabrice Wilhelm, Itziar Oyarzabal, Thomas Lohmiller, Alexander Schnegg, Coen de Graaf, Corine Mathonière, Rodolphe Clérac, and Dawid Pinkowicz

Table of contents:

Description of the crystal structure of [K(crypt-222)]₃[Mo^III(CN)₆]·2CH₃CN (3)

Figure S6. Asymmetric unit of [K(crypt-222)]$_3$[Mo^{III}(CN)$_6$]·2CH$_3$CN (**3**) at 100 K. Ellipsoids are depicted at 50% probability level.

Table S3. Crystal structure parameters for [K(crypt-222)]$_3$[Mo^{III}(CN)$_6$]·2CH$_3$CN (**3**).

Table S4. Selected bond lengths and angles in the structure of [K(crypt-222)]$_3$[Mo^{III}(CN)$_6$]·2CH$_3$CN (**3**) at 100 K.

Figure S7. Experimental powder X-ray diffraction pattern recorded for **3** at 296(2) K (black line) and calculated pattern from the single crystal structure studied at 293(2) K (gray line).

Figure S8. Comparison of the UV-vis spectra of **3** in the solid state (black line) and as a 0.5 mM solution in anhydrous acetonitrile (blue line) at room temperature.

Figure S9. Selected optical reflectivity spectra for **1** between 400 and 1000 nm at selected temperature between 295 and 10 K recorded in the dark and at a scan rate of 4 K min^{-1} in **a**, cooling mode and **b**, heating mode. **c**, Variation of the absolute optical reflectivity (ΔAR) recorded at 550 nm for **1** comparing before and after excitation with different LEDs ($\Delta AR = AR_{after} - AR_{before}$; 10 minutes, at 2 mW cm^{-2}) at 10 K (after a fast cooling of the sample from room temperature in the dark). **d**, Optical reflectivity spectra for **1** at 10 K before and after excitation with a 405-nm LED (10 minutes, at 2 mW·cm^{-2}). **e**, Selected optical reflectivity spectra for **1** at 10 K recorded during a 2-hours irradiation with 405-nm LED (at 5 mW·cm^{-2}). In insert, time evolution of the 550-nm AR signal during 405-nm irradiation (10 K; 5 mW·cm^{-2}). **f**, Thermal variation of the 550-nm reflectivity signal in the dark (in blue, almost temperature independent around 0.2), during irradiation at 10 K with 405 nm LED (2 mW·cm^{-2}; in violet), and after irradiation in the dark (in red). A spectroscopic white light of 0.08 mW·cm^{-2} was used for these measurements.

Figure S10. **a**, Variation of the absolute optical reflectivity (ΔAR) for **1** recorded at 550 nm and at 10 K (after a fast cooling of the sample from room temperature in the dark and a 385-nm excitation during 10 minutes at 2 mW·cm^{-2}) comparing before and after desexcitation with different LEDs ($\Delta AR = AR_{after} - AR_{before}$; 10 minutes, at 10 mW cm^{-2}). **b**, Time evolution of the 550-nm AR signal during four irradiation cycles of 385-nm excitation (10 K; 1 hour, 5 mW·cm^{-2}; in violet) and 660-nm desexcitation (10 K; 2 hours, 10 mW·cm^{-2}; in red). **c**, Selected optical reflectivity spectra for **1** at 10 K recorded in the dark (blue trace), after one 385-nm irradiation (10 K; 1 hour, 5 mW·cm^{-2}; violet trace) and a subsequent 660-nm irradiation (10 K; 2 hours, 10 mW·cm^{-2}; red trace). A spectroscopic white light of 0.08 mW·cm^{-2} was used for these measurements.

Figure S11. a, IR spectrum of **3** recorded in the solid state at room temperature and **b**, close-up of the cyanide stretching region.

Figure S12. Mo L_3-edge XANES spectra at room temperature of **1** in the solid state (solid line) and in water solution (dashed line) (**a**) and **3** in the solid state (solid line) and in the acetonitrile solution (dashed line).

Table S5. Positions and assignments of all excitations from theoretical calculations using CASSCF/CASPT2 (complete active space self consistent field/complete active space perturbation theory) approaches for metal-centered states of **1**.[a]

Table S6. Positions and assignments of all excitations from theoretical calculations using CASSCF/CASPT2 approaches for metal-centered states of **2**.[a]

Details of spin-polarized periodic DFT computations

Table S7. Relative errors in reproducing experimental unit cell volumes (1_{test} for $\Delta V[\mathbf{1}]$ and $\Delta V[\mathbf{2} \rightarrow \mathbf{1}]$, **2** for $\Delta V[\mathbf{1} \rightarrow \mathbf{2}]$ and $\Delta V[\mathbf{2}]$) for studied DFT functionals.

Figure S13. Comparison of Mo···CN distances (for the dissociated CN^- ligand) obtained by geometry optimization of structures **2** and **1**→**2** for studied DFT functionals. Please note that in most cases the circles and squares overlap.

Table S8. Comparison of atomic charges at Mo centers ($Z_{MUL(\alpha-\beta)}$ in a.u.) obtained in the Mulliken population analysis of α-β electrons for studied DFT functionals.

Figure S14. Figure of Merit (defined as described above) obtained by geometry optimization of structures **1**→**2** and **2**→**1** for studied DFT functionals.

Figure S15. Mo···CN distances (blue; right axis) and unit cell volumes (black; left axis) for the optimized geometries of **1**, **1**→**2**, **2** and **2**→**1** for HISS functional.

Figure S16. Overlay of the crystal structures: **a**, experimental **2** (black) and optimized **1**→**2** (blue) and **b**, experimental **1** (black) and optimized **2**→**1** (red), for HISS functional.

Bulk magnetic properties of $K_4[Mo^{III}(CN)_7]\cdot 2H_2O$ (1) in the ground state

Figure S17. a, Temperature (T) dependence of the χT product at 0.1 T for **1** (where $\chi = M/H$ is the molar magnetic susceptibility normalized per complex) and **b**, field (H) dependence of the magnetization (M) for **1** at 1.8 K.

Figure S18. a, Temperature (T) dependence of the molar magnetic susceptibility, χ, at 0.1 T for **1** (black points) and fit to Bonner-Fisher model for a uniform chain of antiferromagnetically coupled $S = 1/2$ Heisenberg spins (green line; *vide supra*). **b**, Temperature dependence of the heat capacity, $C_p(T)$, for **1** under zero magnetic field (open circles), Debye model used to determine the nonmagnetic phonon contribution to the heat capacity ($C_{background}$, red line), and the magnetic contribution to the heat capacity, C_{pm}, defined as $C_p-C_{background}$ (full circles).

Figure S19. Fragments of the crystal structures at 30 K of **1** (a) and **2** (b) highlighting the supramolecular chain arrangement in **1**, and its disappearance in **2** due to the cyanide dissociation.

Bulk magnetic properties of $[K(crypt-222)]_3[Mo^{III}(CN)_6]\cdot 2CH_3CN$ (3)

Figure S20. Temperature (T) dependence of the χT product at 0.1 T for **3** (where $\chi = M/H$ is the molar magnetic susceptibility normalized per complex). The solid purple line is the best fit of the data to a $S = 3/2$ Curie law (with g_{Mo} being the only ajustable parameter).

Figure S21. Field (H) dependence of the magnetization (M) for **3** at 2.0 K. The solid purple line is the simulated $S = 3/2$ Brillouin function with $g_{Mo} = 1.97$.

Table S9. Stretched exponential decay fits of the relaxation data for **2** shown in Fig. 3e.[a]

Figure S22. Photomagnetic studies of 1 after irradiation at 100 K. a, Time evolution of the χT product (at 0.1 T) of **1** during 4 consecutive cycles of 405 nm irradiation at 100 K, each followed by thermal relaxation at 220 K, confirming reversible photo-induced transformation **1→2**; **b**, Temperature dependence of the χT product at 0.1 T before (**1**) and after 405 nm irradiation (**2**) at 100 K in four consecutive irradiation and heating cycles as shown in Fig. S22a; **c**, Magnetization (M) versus magnetic field (H) plots for **1** (before irradiation) and **2** (after 405 nm irradiation) recorded at 2.0 K after four consecutive irradiation and heating cycles as shown in Fig. S22a. Dashed lines in all three plots indicate the χT (**a** and **b**) or M (**c**) values reached after the analogous irradiation experiments performed at 10 K presented in Figure 3.

Referneces

Figure S1. Experimental powder X-ray diffraction pattern obtained for $K_4[Mo^{III}(CN)_7]\cdot2H_2O$ (**1**) at 296(2) K (black line) and the calcuated pattern for the single-crystal structure at 90(2) K (grey line) reported by Ohkoshi et al.[1]
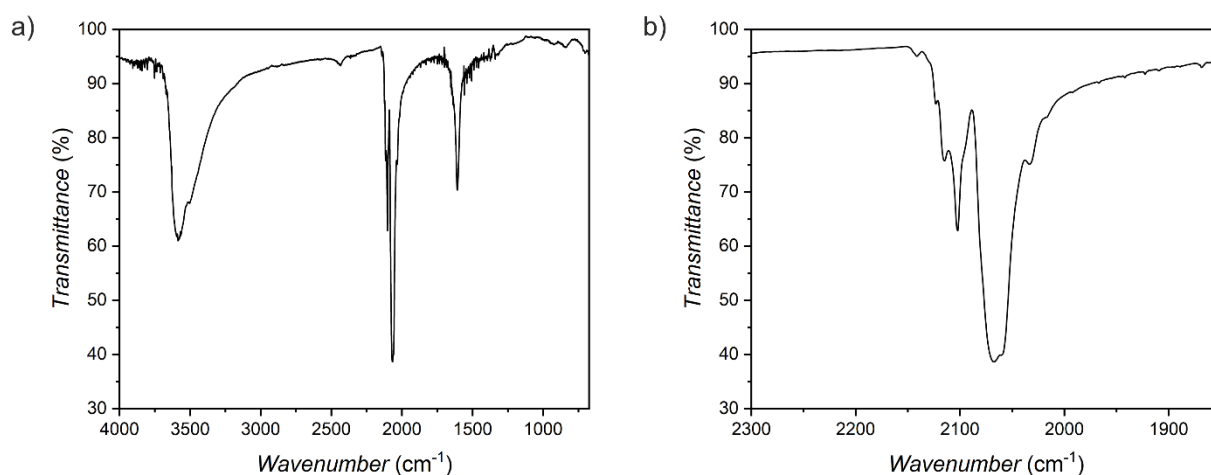

Figure S2. a, Solid state infrared spectrum of **1** recorded at room temperature and **b**, magnification of the 2300-1850 cm^{-1} region of the spectrum showing the cyanide stretching band.

Additional single-crystal X-ray diffraction details

In a preliminary experiment, the initial structure obtained for **1** using synchrotron radiation at 30 K showed a lightly larger unit cell volume of 757.28(9) $Å^3$ (Table S1, **1**test) compared to 752.48(6) $Å^3$ recorded previously at 90 K using a commercial low-flux sealed-tube Mo X-ray source.[1] Repeated measurements on the same single crystal led to a further volume increase of 7 $Å^3$ (up to 764.27(16) $Å^3$, Table S1, **1**test2) and an increase in electron density near the molybdenum ion. These changes were induced by X-ray radiation, and thus the X-ray flux and measurement time were optimized in subsequent experiments to afford the best possible structural parameters with minimal radiation damage.

Table S1. Details of crystal structure measurements and structural refinements.

compound			**1**test	**1**test2
CCDC no.			2352258	2352260
method			single-crystal XRD	single-crystal XRD
formula			$C_7N_7Mo_1K_4O_2H_2$	$C_7N_7Mo_1K_4O_2H_2$
formula weight (g·mol^{-1})			468.50	468.50
T (K)			30(1)	30(1)
λ (Å)			0.6889 (synchrotron)	0.6889 (synchrotron)
crystal system			triclinic	triclinic
space group			$P\bar{1}$	$P\bar{1}$
unit cell		a (Å)	8.9201(5)	8.9957(10)
		b (Å)	9.3166(6)	9.3395(11)
		c (Å)	9.7444(7)	9.7432(12)
		α (deg)	86.900(6)	86.908(11)
		β (deg)	81.977(6)	82.149(11)
		γ (deg)	70.807(6)	70.480(10)
V (Å^3)			757.28(9)	764.27(16)
Z			2	2
calculated density (g·cm^{-3})			2.055	2.036
absorption coefficient (mm^{-1})			1.796	1.779
F(000)			454	454
θ range (deg)			2.244-28.987	2.243-29.071
collected reflections			14359	15513
R_{int}			0.0805	0.0926
completeness (%)			90.6	89.8
data/restraints/parameters			4004 / 3 / 208	4033 / 3 / 208
GOF on F^2			1.013	1.056
final R indices			$R_1 = 0.0501$ [$I > 2\sigma(I)$] $wR_2 = 0.1274$ (all data)	$R_1 = 0.0783$ [$I > 2\sigma(I)$] $wR_2 = 0.1960$ (all data)
largest diff peak and hole			3.829 and -1.219 e·Å^{-3}	6.114 and -2.458 e·Å^{-3}
crystal size (mm x mm x mm)			0.05 x 0.03 x 0.01	0.05 x 0.03 x 0.01

Table S1(cont.). Details of the crystal structure measurements and structural refinements for the first crystal.

compound		**1**	**2**	**1 (relaxed by 638 nm irradiation)**
CCDC no.		2352257	2352263	2352259
method		single-crystal XRD	single-crystal XRD	single-crystal XRD
formula		$C_7N_7Mo_1K_4O_2$	$C_7N_7Mo_1K_4O_2$	$C_7N_7Mo_1K_4O_2$
formula weight (g·mol^{-1})		466.48	468.48	466.48
T (K)		30(1)	30(1)	30(1)
λ (Å)		0.6889 (synchrotron)	0.6889 (synchrotron)	0.6889 (synchrotron)
crystal system		triclinic	triclinic	triclinic
space group		$P\bar{1}$	$P\bar{1}$	$P\bar{1}$
unit cell	**a (Å)**	8.9352(10)	9.598(4)	9.0224(6)
	b (Å)	9.2992(9)	9.710(2)	9.3760(5)
	c (Å)	9.7380(16)	9.752(3)	9.7105(9)
	α (deg)	86.993(12)	66.10(2)	87.576(6)
	β (deg)	82.116(13)	87.91(3)	82.500(7)
	γ (deg)	70.754(9)	88.84(3)	70.809(5)
V (Å^3)		756.67(17)	830.4(5)	769.16(10)
Z		2	2	2
calculated density (g·cm^{-3})		2.047	1.866	2.014
absorption coefficient (mm^{-1})		1.797	1.627	1.757
$F(000)$		450	450	450
θ range (deg)		2.046-28.907	2.058-25.496	2.229-29.077
collected reflections		15026	12741	14567
R_{int}		0.0924	0.1160	0.0881
completeness (%)		0.978	0.976	0.978
data/restraints/parameters		3975/0/200	3306/0/200	4066/24/200
GOF on F^2		1.055	0.995	1.047
final R indices		$R_1 = 0.0579$ $[I > 2\sigma(I)]$ $wR_2 = 0.1501$ (all data)	$R_1 = 0.0567$ $[I > 2\sigma(I)]$ $wR_2 = 0.1446$ (all data)	$R_1 = 0.1087$ $[I > 2\sigma(I)]$ $wR_2 = 0.2703$ (all data)
largest diff peak and hole		4.812 and -1.398 e·Å^{-3}	1.974 and -1.128 e·Å^{-3}	8.236 and -2.888 e·Å^{-3}
crystal size (mm x mm x mm)		0.04 x 0.03 x 0.01	0.04 x 0.03 x 0.01	0.04 x 0.03 x 0.01

Table S1(cont.). Details of crystal structure measurements and structural refinements for the second crystal.

compound		**1′**	**2′**	**1′** **(relaxed by heating to 200 K)**
CCDC no.		2352264	2352261	2352262
method		single-crystal XRD	single-crystal XRD	single-crystal XRD
formula		$C_7N_7Mo_1K_4O_2$	$C_7N_7Mo_1K_4O_2$	$C_7N_7Mo_1K_4O_2$
formula weight (g·mol^{-1})		466.48	466.48	466.48
T (K)		30(1)	30(1)	30(1)
λ (Å)		0.6889 (synchrotron)	0.6889 (synchrotron)	0.6889 (synchrotron)
crystal system		triclinic	triclinic	triclinic
space group		$P\bar{1}$	$P\bar{1}$	$P\bar{1}$
unit cell	**a (Å)**	8.9443(8)	9.6002(9)	8.9697(7)
	b (Å)	9.3385(8)	9.6496(11)	9.3535(6)
	c (Å)	9.7258(11)	9.7097(8)	9.7124(8)
	α (deg)	86.983(9)	65.687(9)	87.317(7)
	β (deg)	82.127(9)	87.767(8)	82.254(7)
	γ (deg)	70.611(8)	88.774(10)	70.731(6)
V (Å^3)		759.04(13)	819.08(15)	762.18(10)
Z		2	2	2
calculated density (g·cm^{-3})		2.041	1.891	2.033
absorption coefficient (mm^{-1})		1.791	1.650	1.784
F(000)		450	450	450
θ range (deg)		2.359-27.338	2.232-27.339	2.051-27.340
collected reflections		14530	15780	14721
R_{int}		0.1065	0.1057	0.1026
completeness (%)		0.976	0.976	0.977
data/restraints/parameters		3635/6/200	3915/6/199	3655/12/200
GOF on F^2		1.060	1.032	1.071
final R indices		$R_1 = 0.0671$ [$I > 2\sigma(I)$] wR_2 = 0.1805 (all data)	$R_1 = 0.0621$ [$I > 2\sigma(I)$] wR_2 = 0.1679 (all data)	$R_1 = 0.0796$ [$I > 2\sigma(I)$] wR_2 = 0.2241 (all data)
largest diff peak and hole		5.131 and -1.495 e·Å^{-3}	3.640 and -0.966 e·Å^{-3}	6.744 and -1.040 e·Å^{-3}
crystal size (mm x mm x mm)		0.04 x 0.03 x 0.01	0.04 x 0.03 x 0.01	0.04 x 0.03 x 0.01

Table S2. Continuous shape measure (CShM) analysis[2] for Mo coordination spheres in the analyzed scXRD structural models. Note that values closer to 0 indicate better agreement with the reference geometry: PBPY-7: pentagonal bipyramid; COC-7: capped octahedron; CTPR-7: capped trigonal prism; PPY-6: pentagonal pyramid; OC-6: octahedron; TPR-6: trigonal prism.
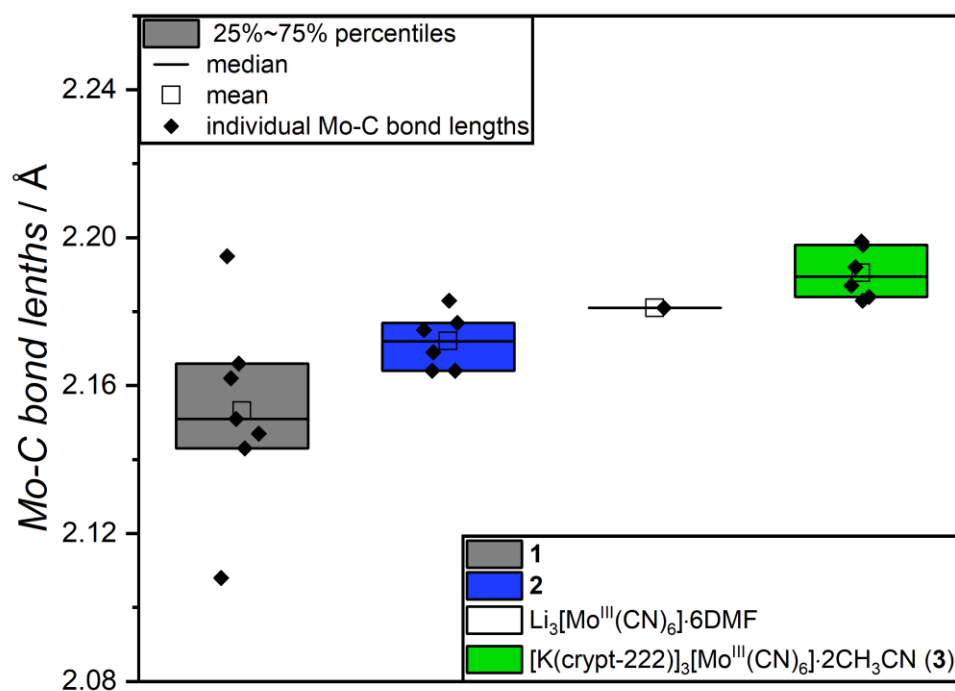
	$[Mo^{III}(CN)_7]^{4-}$		
Structure	**PBPY-7**	**COC-7**	**CTPR-7**
1	5.814	1.534	0.250
1 (relaxed by 638 nm irradiation)	5.735	1.564	0.189
1'	5.729	1.509	0.253
1' (relaxed by heating to 200 K)	5.666	1.549	0.206
	$[Mo^{III}(CN)_6]^{3-}$		
Structure	**PPY-6**	**OC-6**	**TPR-6**
2	27.270	0.213	15.102
2'	27.313	0.202	15.236
3	28.558	0.075	15.496

PBPY-7: pentagonal bipyramid; COC-7: capped octahedron; CTPR-7: capped trigonal prism; PPY-6: pentagonal pyramid; OC-6: octahedron; TPR-6: trigonal prism

Figure S3. Mo-C bond length analysis in **1**, **2**, Li$_3$[Mo^{III}(CN)$_6$]·6DMF [3] and [K(crypt-222)]$_3$[Mo^{III}(CN)$_6$]·2CH$_3$CN (**3**).
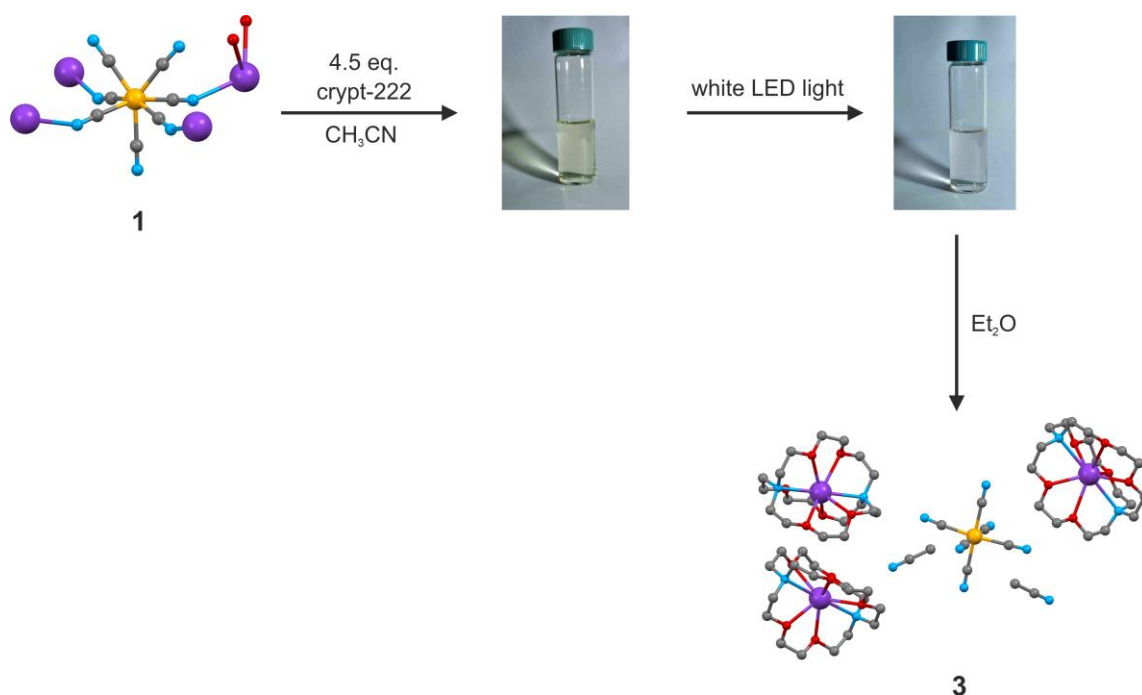
Figure S4. Schematic representation of the photochemical transformation from **1** to **3** in acetonitrile solution at room temperature.
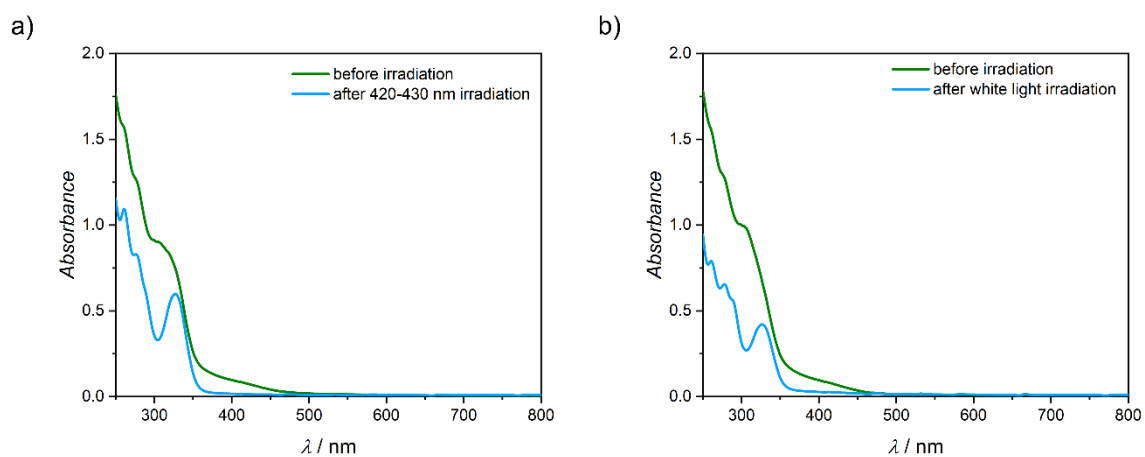

Figure S5. UV-vis spectra for 0.5 mM solutions of **1** in CH$_3$CN (solubilized with four equivalents of crypt-222) recorded at room temperature before irradiation (green line) and after irradiation (blue line): **a**, after 20 minutes of violet light irradiation (λ = 420-430 nm) and **b**, 5 minutes of white LED light irradiation.

Description of the crystal structure of [K(crypt-222)]$_3$[Mo^{III}(CN)$_6$]·2CH$_3$CN (3)

Compound **3** crystallizes in the orthorhombic *Pbca* space group, with the asymmetric unit corresponding to the empirical formula, [K(crypt-222)]$_3$[Mo^{III}(CN)$_6$]·2CH$_3$CN (Table S3). In its crystal structure, the [Mo^{III}(CN)$_6$]$^{3-}$ anion is surrounded by three [K(crypt-222)]$^+$ cations and two acetonitrile molecules as crystallization solvents (Fig. S6 – asymmetric unit). The hexacyanomolybdate(III) anion interacts through weak C-H···N contacts with methylene groups of [K(crypt-222)]$^+$ cations and with methyl groups of acetonitrile, effectively isolating each [Mo^{III}(CN)$_6$]$^{3-}$ unit. Similar to Li$_3$[Mo^{III}(CN)$_6$]·6DMF, the hexacyanomolybdate(III) anion in **3** exhibits nearly ideal octahedral geometry, as confirmed by continuous symmetry measures using the SHAPE software (Table S2).[2] The average Mo-C bond length in **3** is 2.191(6) Å at 100 K (Table S4), closely matching the 2.181(3) Å observed for the lithium salt at room temperature (Fig. S3). These structural parameters for [Mo^{III}(CN)$_6$]$^{3-}$ in **3** serve as a benchmark for comparison with the photoinduced state in **2**. Notably, the lengthening of the Mo-C bonds in **1** from 2.153(18) Å to 2.172(6) in **2** (and from 2.156(19) Å to 2.188(11) Å in the second crystal) aligns well with the 2.191(6) Å seen in **3**. This structural evidence supports the photoinduced tranformation scheme [Mo^{III}(CN)$_7$]$^{4-}$ → [Mo^{III}(CN)$_6$]$^{3-}$ + CN$^-$, further corroborated by spectroscopic and magnetic analyses.
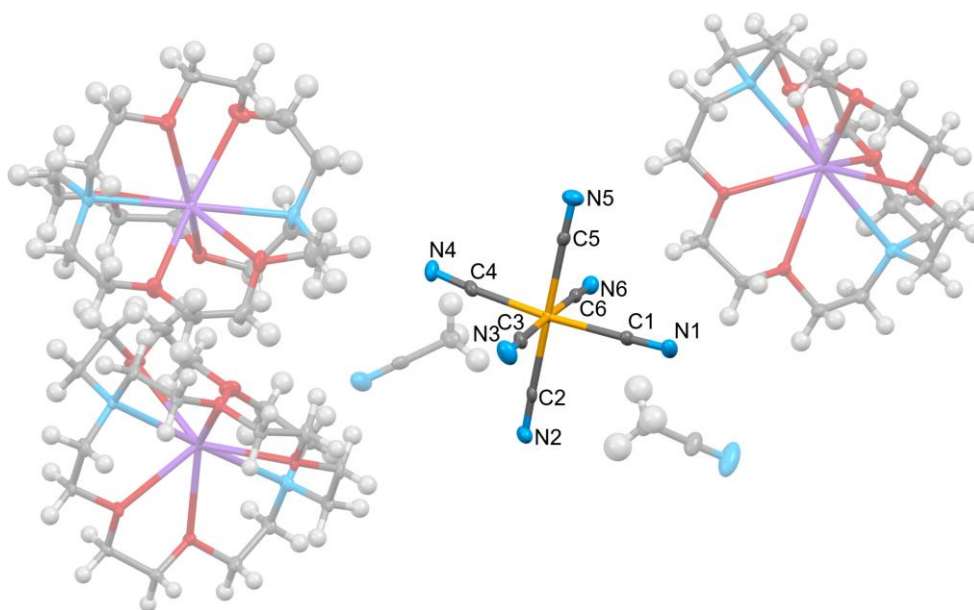
Figure S6. Asymmetric unit of [K(crypt-222)]$_3$[Mo^{III}(CN)$_6$]·2CH$_3$CN (**3**) at 100 K. Ellipsoids are depicted at 50% probability level.

Table S3. Crystal structure parameters for [K(crypt-222)]$_3$[Mo^{III}(CN)$_6$]·2CH$_3$CN (**3**).

compound		**3** (100 K)	**3** (293 K)
CCDC no.		2352265	2352266
method		single-crystal XRD	single-crystal XRD
formula		C$_{64}$H$_{114}$K$_3$MoN$_{14}$O$_{18}$	C$_{64}$H$_{114}$K$_3$MoN$_{14}$O$_{18}$
formula weight (g·mol^{-1})		1580.93	1580.93
T (K)		100(2)	293(2)
λ (Å)		0.7107 (Mo Kα)	0.7107 (Mo Kα)
crystal system		orthorhombic	orthorhombic
space group		*Pbca*	*Pbca*
unit cell	**a (Å)**	18.2778(5)	18.4282(14)
	b (Å)	20.0943(6)	20.1869(18)
	c (Å)	43.6202(11)	43.971(4)
V (Å^3)		16020.8(8)	16358(2)
Z		8	8
calculated density (g·cm^{-3})		1.311	1.284
absorption coefficient (mm^{-1})		0.39	0.38
F(000)		6712	6712
θ range (deg)		2.4-27.9	2.7-23.4
collected reflections		154424	150923
R_{int}		0.061	0.132
completeness (%)		99.8	98.4
data/restraints/parameters		19084 / 0 / 903	14756 / 70 / 903
GOF on F^2		1.20	1.05
final R indices		R_1 = 0.067 [$I > 2\sigma(I)$] wR_2 = 0.124 (all data)	R_1 = 0.081 [$I > 2\sigma(I)$] wR_2 = 0.187 (all data)
largest diff peak and hole		1.20 and -1.65 e·Å^{-3}	1.00 and -1.13 e·Å^{-3}
crystal size (mm x mm x mm)		0.40 x 0.30 x 0.16	0.36 x 0.26 x 0.10

Table S4. Selected bond lengths and angles in the structure of [K(crypt-222)]$_3$[Mo^{III}(CN)$_6$]·2CH$_3$CN (**3**) at 100 K.

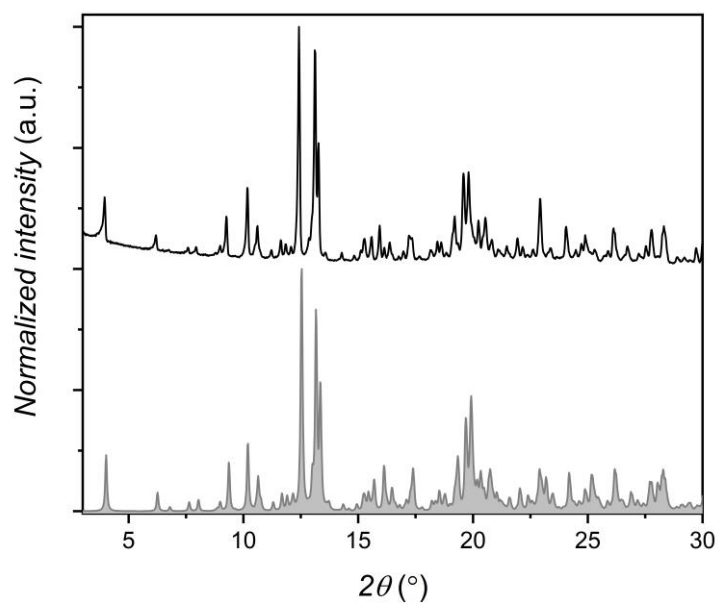| Bonds / Å		Angles / °	
Mo-C1	2.187(3)	Mo-C1-N1	177.3(3)
Mo-C2	2.199(3)	Mo-C2-N2	177.3(3)
Mo-C3	2.198(3)	Mo-C3-N3	179.0(3)
Mo-C4	2.183(3)	Mo-C4-N4	175.8(3)
Mo-C5	2.184(3)	Mo-C5-N5	179.0(3)
Mo-C6	2.192(3)	Mo-C6-N6	179.1(3)
Mo-C average	2.191(6)	Mo-C-N average	177.9(11)
Angles / °			
C1-Mo-C2	91.39(11)	C1-Mo-C4	174.39(11)
C1-Mo-C3	91.03(12)	C2-Mo-C5	177.99(11)
C1-Mo-C5	88.66(11)	C3-Mo-C6	178.23(12)
C1-Mo-C6	87.84(11)		
C2-Mo-C3	91.21(11)		
C2-Mo-C4	92.34(12)		
C2-Mo-C6	87.47(11)		
C3-Mo-C4	93.08(12)		
C3-Mo-C5	90.80(11)		
C4-Mo-C5	87.47(11)		
C4-Mo-C6	88.14(11)		
C5-Mo-C6	90.52(11)		

Figure S7. Experimental powder X-ray diffraction pattern recorded for **3** at 296(2) K (black line) and calculated pattern from the single crystal structure studied at 293(2) K (gray line).
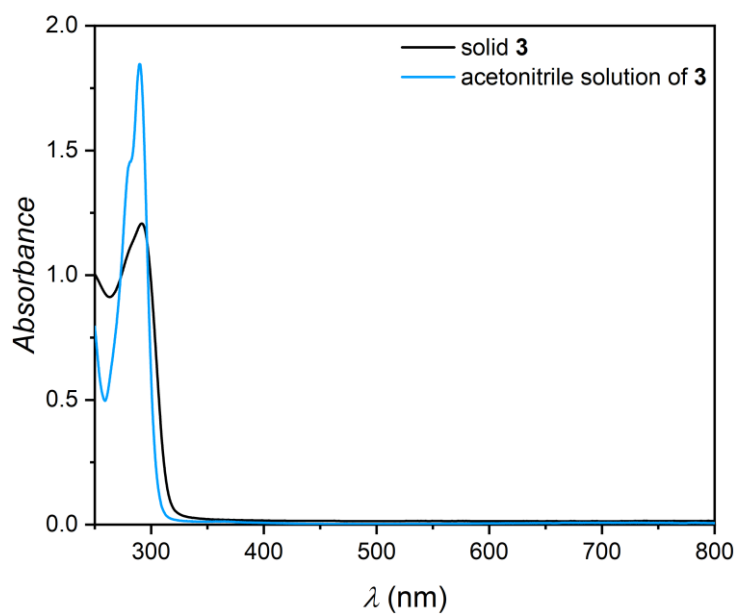

Figure S8. Comparison of the UV-vis spectra of **3** in the solid state (black line) and as a 0.5 mM solution in anhydrous acetonitrile (blue line) at room temperature.
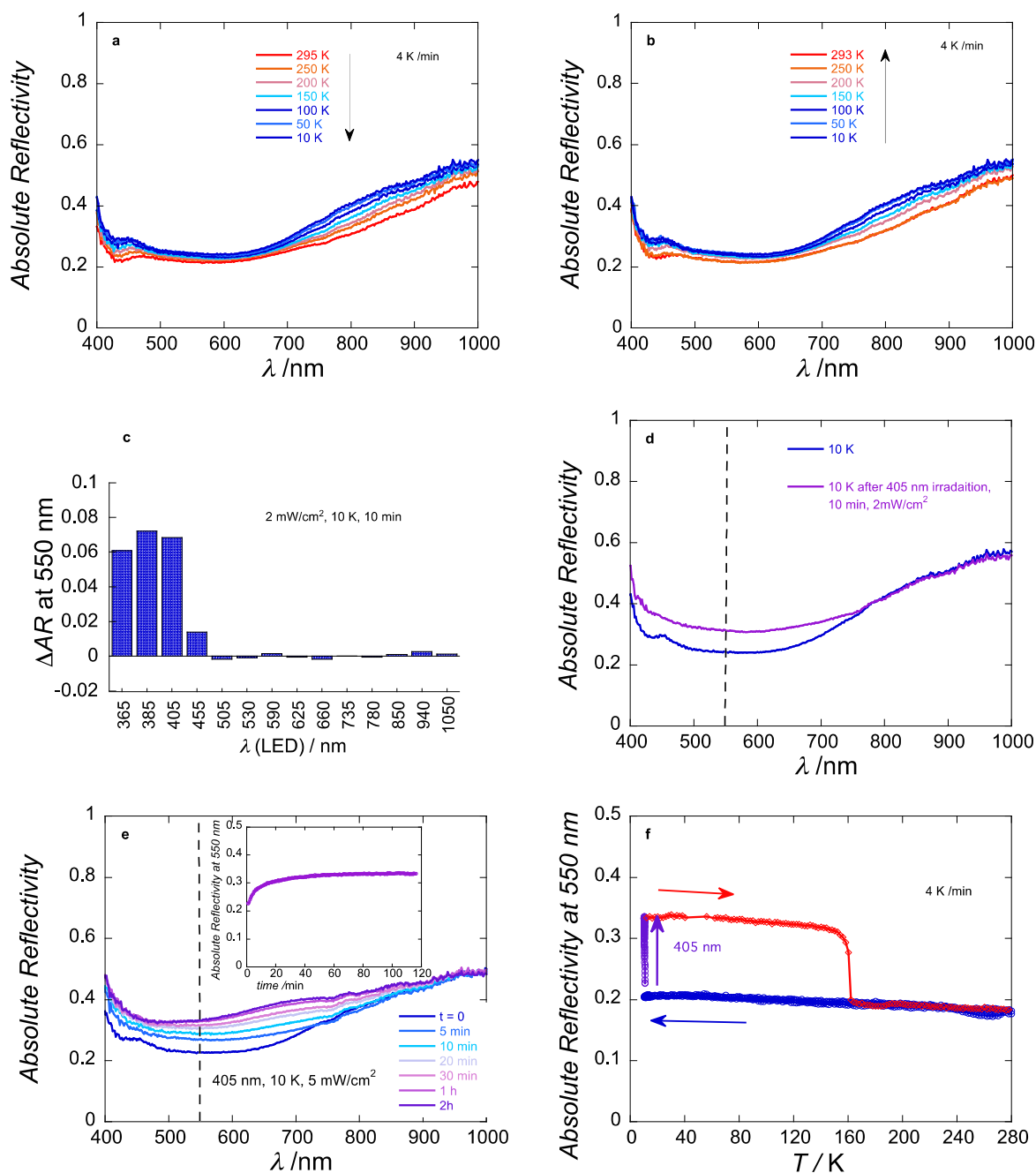
Figure S9. Selected optical reflectivity spectra for **1** between 400 and 1000 nm at selected temperature between 295 and 10 K recorded in the dark and at a scan rate of 4 K min^{-1} in **a**, cooling mode and **b**, heating mode. **c**, Variation of the absolute optical reflectivity (ΔAR) recorded at 550 nm for **1** comparing before and after excitation with different LEDs ($\Delta AR = AR_{after} - AR_{before}$; 10 minutes, at 2 mW cm^{-2}) at 10 K (after a fast cooling of the sample from room temperature in the dark). **d**, Optical reflectivity spectra for **1** at 10 K before and after excitation with a 405-nm LED (10 minutes, at 2 mW·cm^{-2}). **e**, Selected optical reflectivity spectra for **1** at 10 K recorded during a 2-hours irradiation with 405-nm LED (at 5 mW·cm^{-2}). In insert, time evolution of the 550-nm AR signal during 405-nm irradiation (10 K; 5 mW·cm^{-2}). **f**, Thermal variation of the 550-nm reflectivity signal in the dark (in blue, almost temperature independent around 0.2), during irradiation at 10 K with 405 nm LED (2 mW·cm^{-2}; in violet), and after irradiation in the dark (in red). A spectroscopic white light of 0.08 mW·cm^{-2} was used for these measurements.
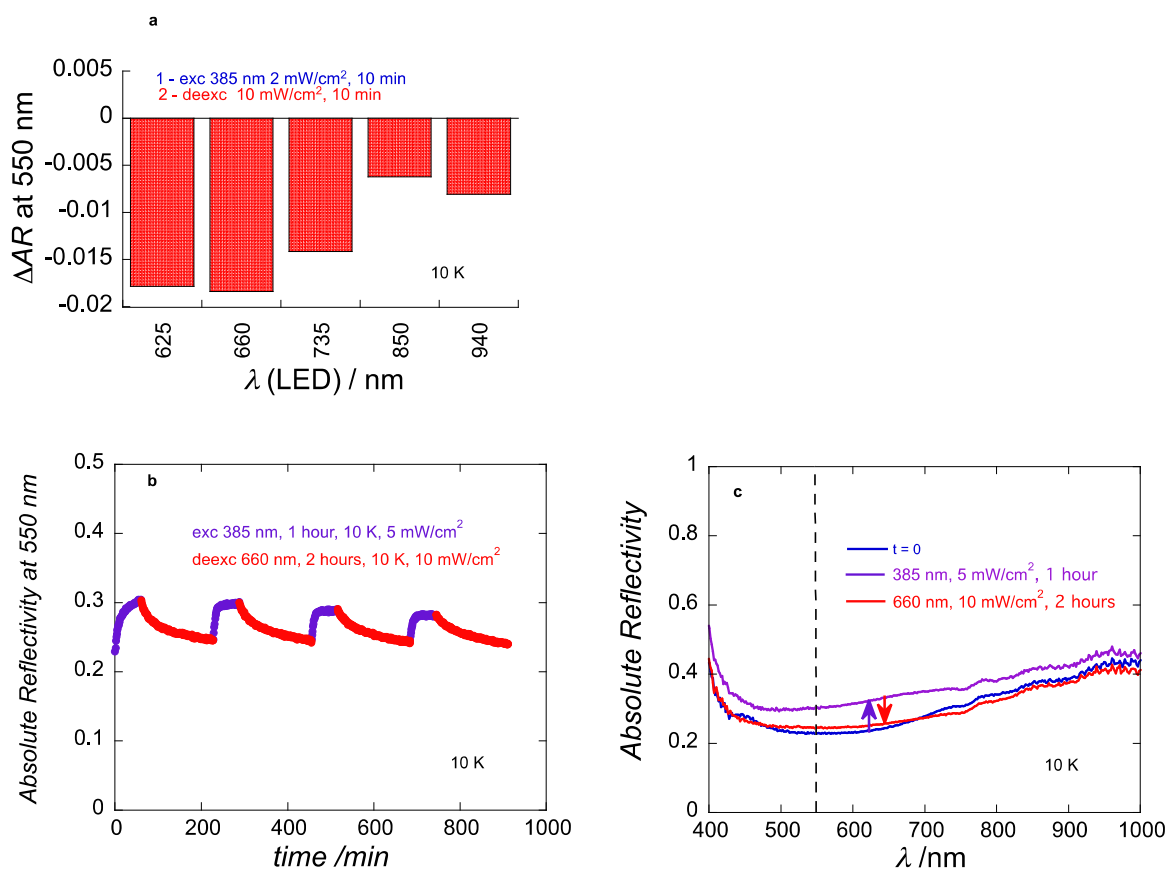
15

Figure S10. **a**, Variation of the absolute optical reflectivity (ΔAR) for **1** recorded at 550 nm and at 10 K (after a fast cooling of the sample from room temperature in the dark and a 385-nm excitation during 10 minutes at 2 mW·cm^{-2}) comparing before and after desexcitation with different LEDs ($\Delta AR = AR_{after} - AR_{before}$; 10 minutes, at 10 mW cm^{-2}). **b**, Time evolution of the 550-nm AR signal during four irradiation cycles of 385-nm excitation (10 K; 1 hour, 5 mW·cm^{-2}; in violet) and 660-nm desexcitation (10 K; 2 hours, 10 mW·cm^{-2}; in red). **c**, Selected optical reflectivity spectra for **1** at 10 K recorded in the dark (blue trace), after one 385-nm irradiation (10 K; 1 hour, 5 mW·cm^{-2}; violet trace) and a subsequent 660-nm irradiation (10 K; 2 hours, 10 mW·cm^{-2}; red trace). A spectroscopic white light of 0.08 mW·cm^{-2} was used for these measurements.
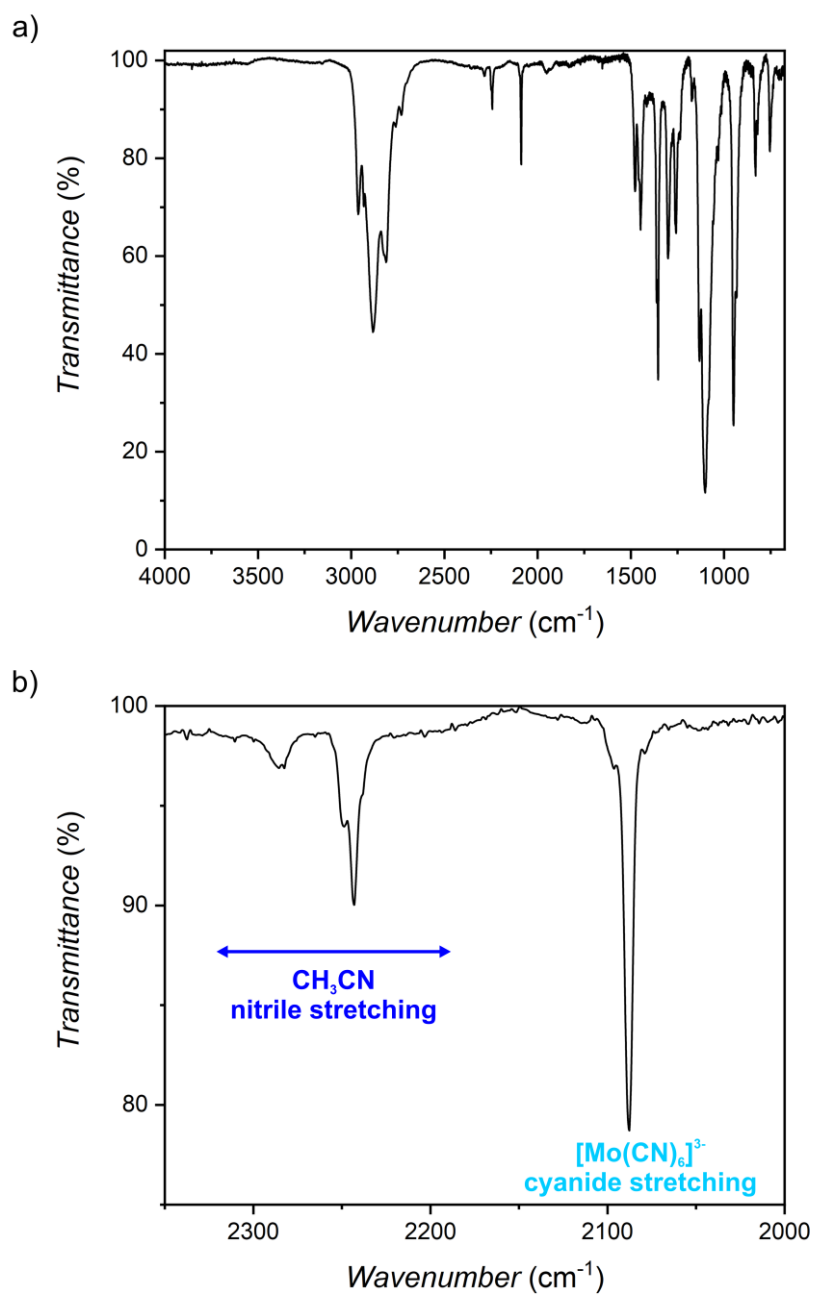
Figure S11. a, IR spectrum of **3** recorded in the solid state at room temperature and **b**, close-up of the cyanide stretching region.

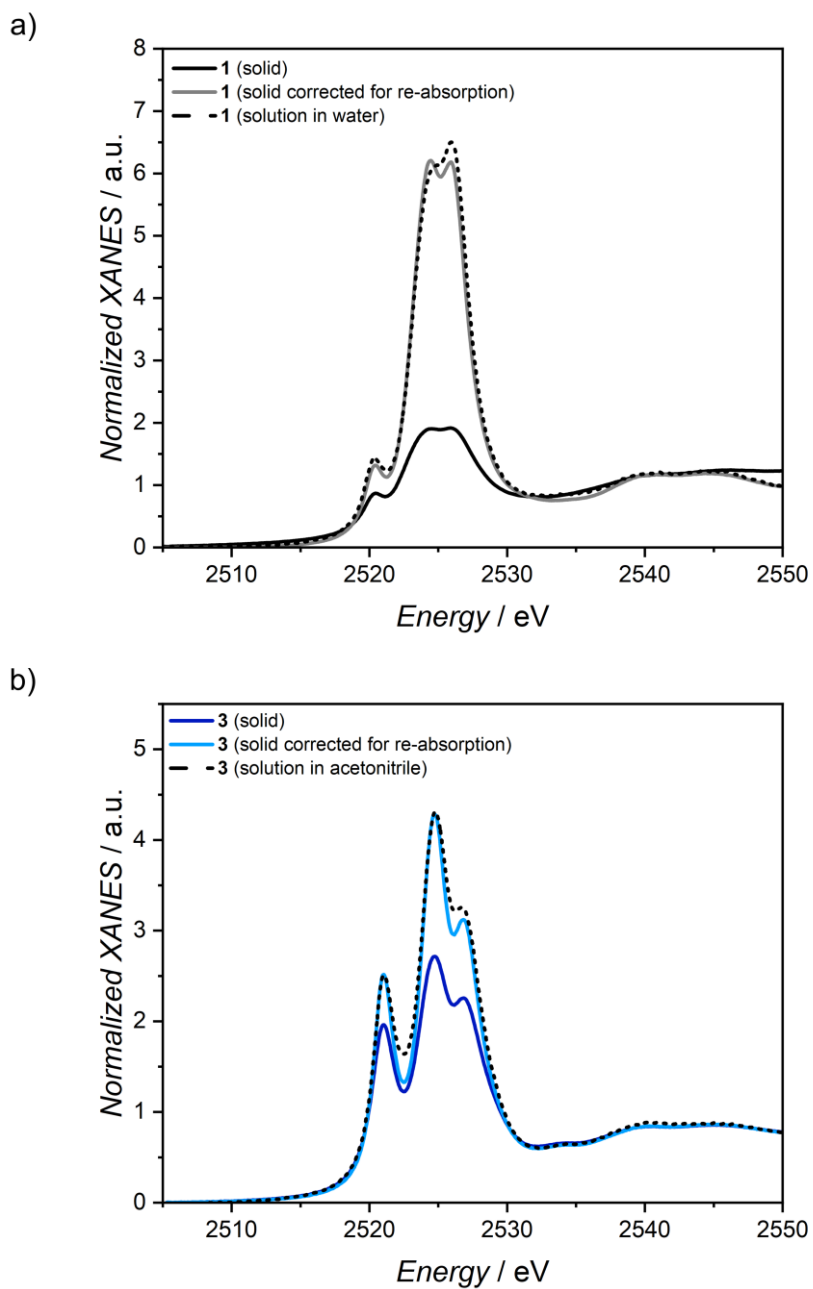a)

b)

Figure S12. Mo L_3-edge XANES spectra at room temperature of **1** in the solid state (solid line) and in water solution (dashed line) (**a**) and **3** in the solid state (solid line) and in the acetonitrile solution (dashed line).

Table S5. Positions and assignments of all excitations from theoretical calculations using CASSCF/CASPT2 (complete active space self consistent field/complete active space perturbation theory) approaches for metal-centered states of **1**.[a]

State	CASSCF (eV)	CASPT2 (eV)	CASSCF (nm)	CASPT2 (nm)
MC	0.00	0.00	---	---
MC	0.28	0.30	---	---
MC	2.31	2.69	536.7	460.9
MC	2.89	3.32	429.0	373.4
MC	3.23	3.43	383.9	361.5
MC	3.40	3.60	364.7	344.4
MC	3.42	3.61	362.5	343.4
MC	3.71	4.12	334.2	300.9
MC	3.79	4.07	327.1	304.6
MC	3.84	4.08	322.9	303.9
MC	4.14	4.32	299.5	287.0
MC	4.28	4.38	289.7	283.1
MC	4.62	4.84	268.4	256.2
MC	4.70	4.90	263.8	253.0
MC	5.23	5.22	237.1	237.5
MC	5.52	5.42	224.6	228.8
LMCT	5.95	4.79	208.4	258.8
LMCT/MC	6.04	5.52	205.3	224.6
LMCT	6.30	4.63	196.8	267.8
MC	6.45	7.09	192.2	174.9
MC	6.84	7.49	181.3	165.5
MC/π-π*	7.00	6.82	177.1	181.8
MC	7.08	7.72	175.1	160.6
MC	7.13	7.64	173.9	162.3
MC/π-π*	7.26	7.05	170.8	175.9
MC	7.36	7.76	168.5	159.8
MC	7.41	7.95	167.3	156.0
MC	7.45	7.85	166.4	157.9
MC	7.59	8.06	163.4	153.8
MC	7.74	8.29	160.2	149.6
MC	7.85	8.48	157.9	146.2
MC	7.85	8.29	157.9	149.6
MC	7.90	8.33	156.9	148.8

[a]quartet states (S = 3/2) are marked with blue background; MC: metal centered; LMCT: ligand metal charge transfer.

Table S6. Positions and assignments of all excitations from theoretical calculations using CASSCF/CASPT2 approaches for metal-centered states of **2**.[a]

State	CASSCF (eV)	CASPT2 (eV)	CASSCF (nm)	CASPT2 (nm)
$^4A_{2g}$	0	0	---	---
$^2E_g\,(t^3)$	1.10	1.29	1127.1	961.1
	1.10	1.30	1127.1	953.7
$^2T_{1g}\,(t^3)$	1.15	1.34	1078.1	925.3
	1.16	1.35	1068.8	918.4
	1.17	1.34	1059.7	925.3
$^2T_{2g}\,(t^3)$	2.06	2.05	601.9	604.8
	2.09	2.11	593.2	587.6
	2.09	2.11	593.2	587.6
$^4T_{2g}$	4.68	5.07	264.9	244.5
	4.69	5.08	264.4	244.1
	4.72	5.18	262.7	239.4
$^4T_{1g}$	5.45	5.74	227.5	216.0
	5.51	5.80	225.0	213.8
$^2A_{1g}\,(t^2e^1)$	5.51	6.05	225.0	204.9
LMCT/π-π*	5.53	4.81	224.2	257.8
other t^2e^1 doublets	5.64	6.19	219.8	200.3
	5.67	6.22	218.7	199.3
	5.68	6.22	218.3	199.3
$^4T_{1g}$	5.76	6.06	215.3	204.6
other t^2e^1 doublets	5.77	6.28	214.9	197.4
	5.78	6.30	214.5	196.8
	5.79	6.29	214.1	197.1
LMCT	5.86	5.17	211.6	239.8
other t^2e^1 doublets	5.93	6.38	209.1	194.3
	5.99	6.42	207.0	193.1
	6.22	6.62	199.3	187.3
	6.25	6.65	198.4	186.4

[a]doublet states are marked with an orange background.

Details of spin-polarized periodic DFT computations

To reproduce the structural transformations from **1** to **2** and back, a computational protocol was developed involving various optimization approaches and density functionals. Three hybrid functionals (PBE0[4, 5] PBE0-13[6], and B3LYP[7-9]) and four range-separated hybrid functionals (LC-PBE,[4, 10, 11] LC-ωPBE,[4, 12] HISS,[13, 14] and CAM-B3LYP[7, 8, 15]) were tested. The D3 dispersion correction with Becke–Johnson damping function was applied for PBE0, B3LYP, and LC-ωPBE.[14, 15] The protocol included two optimization types in CRYSTAL23[16] – full optimization of unit cell parameters and atom positions (FO) and optimization of atom positions within a fixed unit cell (AO). Initial models, based on scXRD data with added hydrogen atoms (positionned at electron density maxima according to chemical criteria), were optimized using AO and FO to simulate spin-state transformations, **1→2** and **2→1**. FO re-optimization then used a spin-lock to fix the (α-β) electron occupancy matching the target spin state during the first 50 SCF (self consisten field) cycles. Transitions were simulated in both preserved and reduced symmetry ($P\bar{1}$ and P1) to determine if symmetry breaking is part of the transformations. Results were evaluated by comparing experimental and computed structural parameters (e.g., unit cell, Mo···CN distances) and spin density at the Mo centers, estimated according to the atomic charges ($Z_{MUL(α-β)}$) obtained in the Mulliken population analysis of α-β electrons.[17] To test internal consistency, a Figure of Merit (FoM) parameter was defined for calculations using each functional:

$$FoM = \frac{V[\boldsymbol{a} \rightarrow \boldsymbol{b}] - V[\boldsymbol{b}]}{V[\boldsymbol{b}]}$$

where the unit cell volumes $V[\boldsymbol{a}\rightarrow\boldsymbol{b}]$ and $V[\boldsymbol{b}]$ represent $V[\mathbf{1}\rightarrow\mathbf{2}]$ and $V[\mathbf{2}]$ for a **1→2** transformation, and $V[\mathbf{2}\rightarrow\mathbf{1}]$ and $V[\mathbf{1}]$ for a **2→1** transformation. As such, a FoM should be equal to zero if the transformation induced by the spin-lock procedure perfectly replicates the target spin state's optimized geometry. Evaluating these parameters across functionals showed no significant differences between calculations in $P\bar{1}$ and $P1$ symmetry. Additionally, re-optimization from both AO and FO geometries yielded nearly identical results, despite different starting unit cell parameters and coordinates. Consequently, only FO $P\bar{1}$ results are discussed further.

Given that structural models were based on 30 K scXRD measurements, accurate reproduction of unit cell parameters and volume was anticipated for both optimized spin states. Depending on the DFT functional, results showed either contraction or inflation of the unit cells (Table S7). Functionals underestimating volume tended to replicate the smaller unit cell of **1** more accurately, while those overestimating better reproduced $V[\mathbf{2}]$. The PBE0-D3 and HISS functionals yielded the closest volumes for **1** and **2**, respectively. For **2**, the Mo···CN distance in the dissociated cyanide correlated well with the optimized unit cell size, with HISS almost perfectly matching the experimental distance (Fig. S13, Table S7). Comparison of $Z_{MUL(α-β)}$ values at the Mo centers (Table S8) highlighted the range-separated functionals as superior in capturing the expected number of unpaired electrons for each spin state.

Each functional successfully replicated the **1→2** structural transformation when the spin-lock procedure was applied. In all cases, one cyanide group dissociated from the Mo center early in re-optimization, stabilizing through two nearly linear hydrogen bonds with water molecules. For each functional, unit cell volume, $Z_{MUL(α-β)}$ values at the Mo centers, and the position of the dissociated CN⁻ resulting from the re-optimization of **1** are almost identical to that obtained after the optimization of **2** starting from the experimental data (Table S7-S8, Fig. S13-S14). However, only PBE-based functionals reproduced the reverse **2→1** transformation (Table S8). For B3LYP and CAM-B3LYP, the structure did not shift to a smaller volume, and CN⁻ association was absent (Table S7, Fig. S14). Overall, the HISS DFT functional provided the best alignment with experimental data (Fig. S15-S16).

Table S7. Relative errors in reproducing experimental unit cell volumes (1_{test} for $\Delta V[1]$ and $\Delta V[2{\rightarrow}1]$, 2 for $\Delta V[1{\rightarrow}2]$ and $\Delta V[2]$) for studied DFT functionals.

Method	$\Delta V[1]$ (%)	$\Delta V[1{\rightarrow}2]$ (%)	$\Delta V[2]$ (%)	$\Delta V[2{\rightarrow}1]$ (%)
B3LYP-D3	-0.95	-3.11	-2.96	5.87*
CAM-B3LYP	4.05	1.95	1.96	11.47*
LC-PBE	-2.59	-5.06	-5.11	-3.10
LC-ωPBE-D3	-2.25	-4.58	-4.56	-2.27
PBE0-D3	-0.78	-3.02	-2.99	-0.79
PBE0-13	3.96	2.06	2.09	3.94
HISS	2.93	0.95	0.96	2.93

*6-coordinate Mo centers
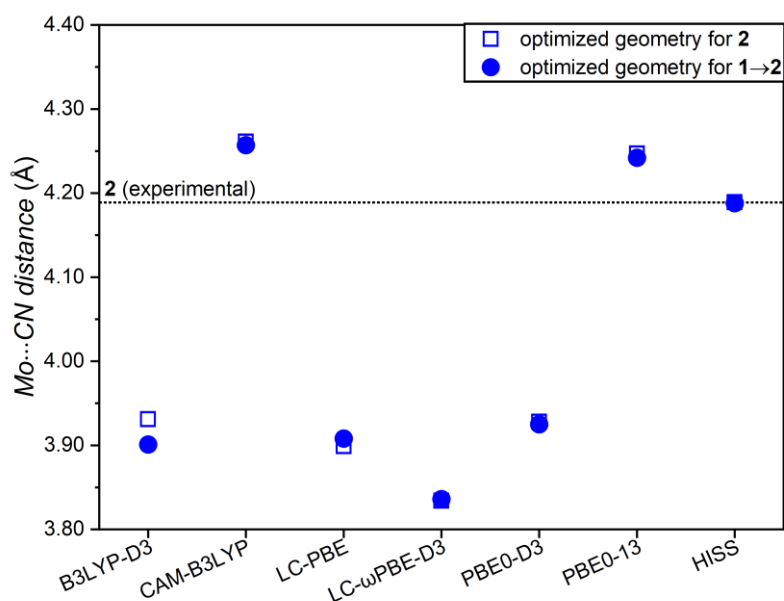
Figure S13. Comparison of Mo···CN distances (for the dissociated CN⁻ ligand) obtained by geometry optimization of structures **2** and **1→2** for studied DFT functionals. Please note that in most cases the circles and squares overlap.

Table S8. Comparison of atomic charges at Mo centers ($Z_{MUL(\alpha-\beta)}$ in a.u.) obtained in the Mulliken population analysis of α-β electrons for studied DFT functionals.

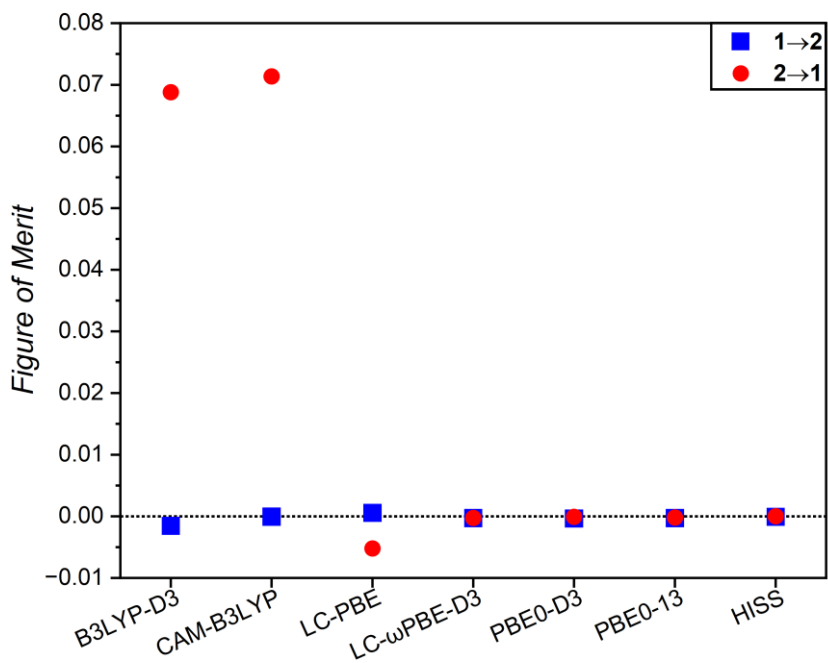| Method	$Z_{MUL(\alpha-\beta)}[1]$ (a.u.)	$Z_{MUL(\alpha-\beta)}[1{\rightarrow}2]$ (a.u.)	$Z_{MUL(\alpha-\beta)}[2]$ (a.u.)	$Z_{MUL(\alpha-\beta)}[2{\rightarrow}1]$ (a.u.)
B3LYP-D3	0.833	2.710	2.711	0.898*
CAM-B3LYP	0.900	2.841	2.841	0.950*
LC-PBE	0.920	2.920	2.920	0.935
LC-ωPBE-D3	0.923	2.929	2.929	0.923
PBE0-D3	0.850	2.774	2.774	0.850
PBE0-13	0.893	2.855	2.855	0.893
HISS	0.910	2.888	2.888	0.910

*6-coordinate Mo centers

Figure S14. Figure of Merit (defined as described above) obtained by geometry optimization of structures **1→2** and **2→1** for studied DFT functionals.
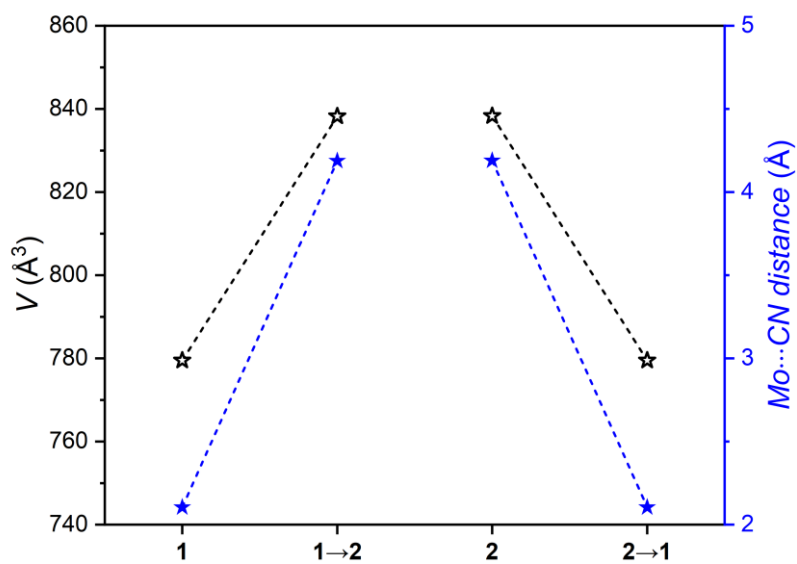

Figure S15. Mo···CN distances (blue; right axis) and unit cell volumes (black; left axis) for the optimized geometries of **1**, **1→2**, **2** and **2→1** for HISS functional.
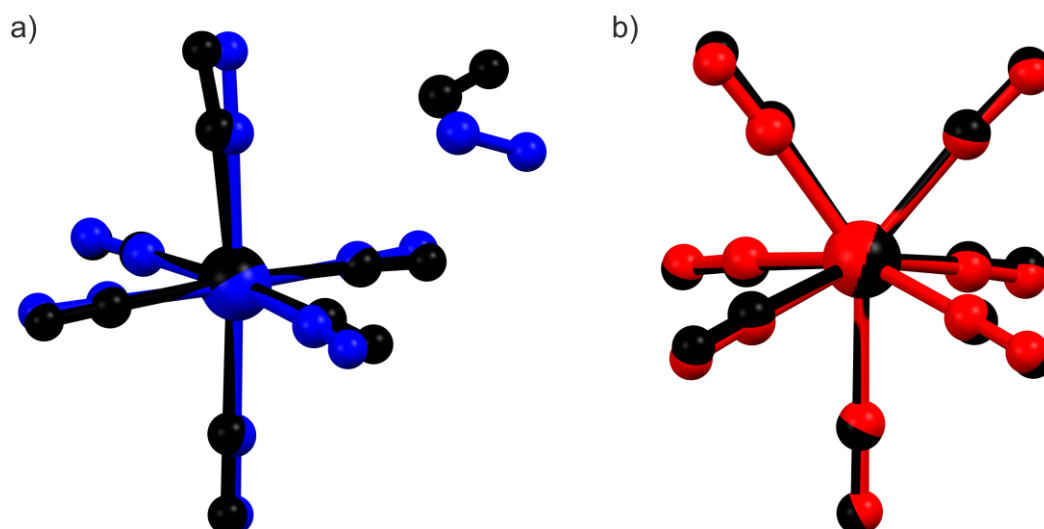
Figure S16. Overlay of the crystal structures: **a**, experimental **2** (black) and optimized **1→2** (blue) and **b**, experimental **1** (black) and optimized **2→1** (red), for HISS functional.

Bulk magnetic properties of K$_4$[Mo^{III}(CN)$_7$]·2H$_2$O (1) in the ground state

The magnetic susceptibility (χ) of **1** was analysed using the Bonner-Fisher model for a uniform chain of antiferromagnetically coupled $S = 1/2$ Heisenberg spins (Fig. S18a):[18, 19]

$$\hat{H} = -2J \sum_{i=1}^{N} \vec{S}_i \cdot \vec{S}_{i+1} - g\mu_B \sum_{i=1}^{N} \vec{H} \cdot \vec{S}_i$$

Assuming $S = 1/2$ molybdenum centers and utilizing g-factors derived from EPR spectroscopy, the isotropic superexchange coupling was found to be J/k_B = -4.2(1) K (fitting temperature range 2-300 K). This model aligns well with the crystal structure of **1**, where the N1···N7 distance of 3.40(1) Å is the smallest separation among heptacyanomolybdate(III) complexes, facilitating th150
e formation of a supramolecular chain (Fig. S19). Furthermore, intermolecular interactions are mediated by CN···K···NC bridges, supporting the description via a superexchange mechanism. However, the model does not adequately account for the magnetic susceptibility below 15 K, likely due to interchain interactions in a densely packed structure of **1** and the presence of an antiferromagnetically ordered state below 3.5 K (vide infra).

The heat capacity (C_p) measurements reveal a broad maximum at 3.5 K which is lower than the magnetic susceptibility (χ) maximum at 5.5 K (Fig. S18). This is consistent with the low dimensionality of **1** and its supramolecular spin chain arrangement.[18] The magnetic entropy change associated to this C_p peak, after subtracting the phonon contribution (red line in Fig. S18 b), is approximately ΔS = 4.9 J·K^{-1}·mol^{-1} in the 0.5-10 K range. This value is only slightly lower than the expected Rln 2 = 5.76 J·K^{-1}·mol^{-1} for an ordered $S = \frac{1}{2}$ system. These correlations reduce the experimentally determined ΔS and contribute to the absence of a sharp lambda-shaped peak in the specific heat at the magnetic transition.
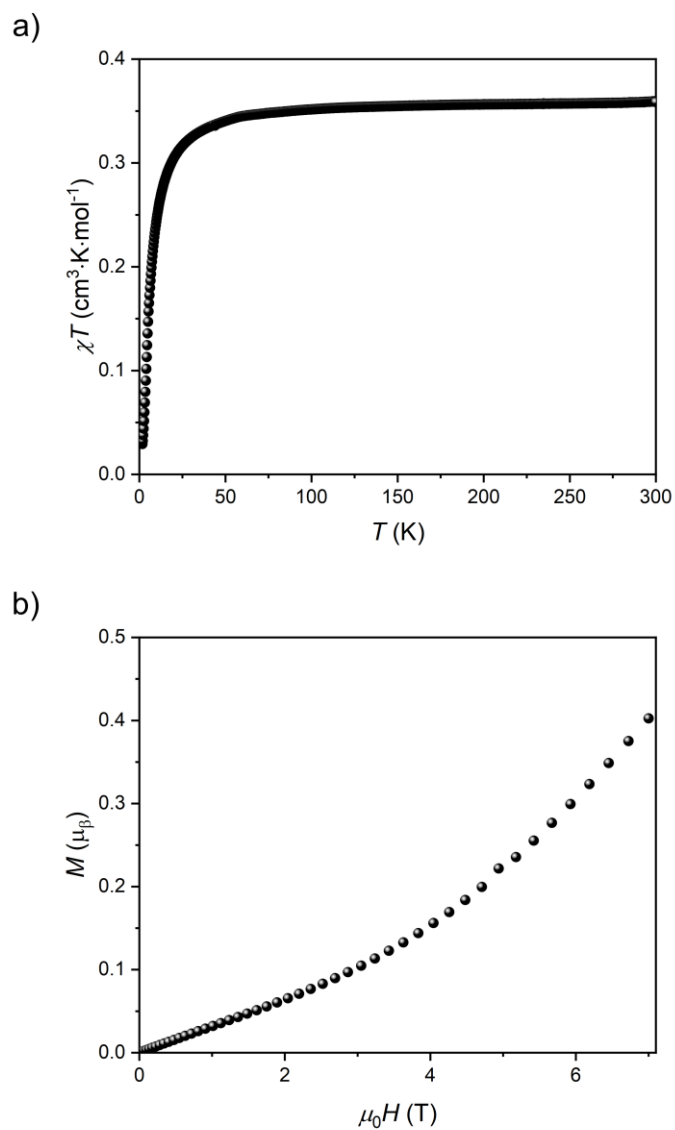
a)

b)

Figure S17. a, Temperature (T) dependence of the χT product at 0.1 T for **1** (where $\chi = M/H$ is the molar magnetic susceptibility normalized per complex) and **b**, field (H) dependence of the magnetization (M) for **1** at 1.8 K.
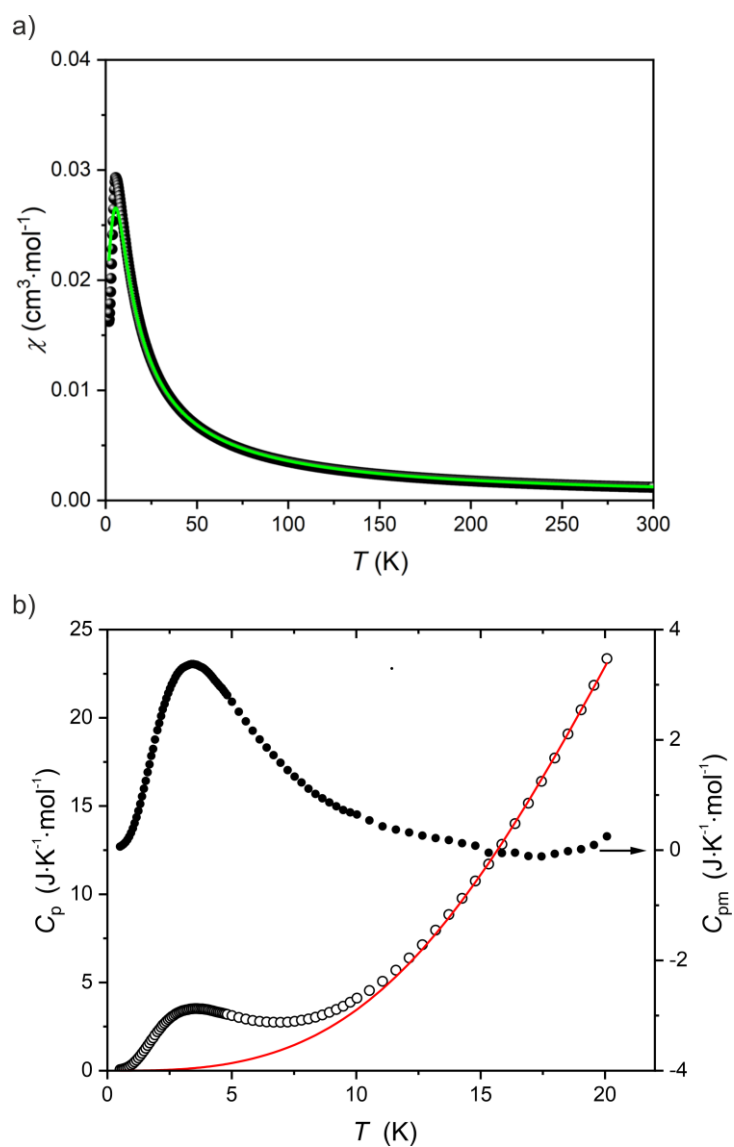
Figure S18. a, Temperature (T) dependence of the molar magnetic susceptibility, χ, at 0.1 T for **1** (black points) and fit to Bonner-Fisher model for a uniform chain of antiferromagnetically coupled $S = 1/2$ Heisenberg spins (green line; *vide supra*). **b**, Temperature dependence of the heat capacity, $C_p(T)$, for **1** under zero magnetic field (open circles), Debye model used to determine the nonmagnetic phonon contribution to the heat capacity ($C_{background}$, red line), and the magnetic contribution to the heat capacity, C_{pm}, defined as C_p-$C_{background}$ (full circles).
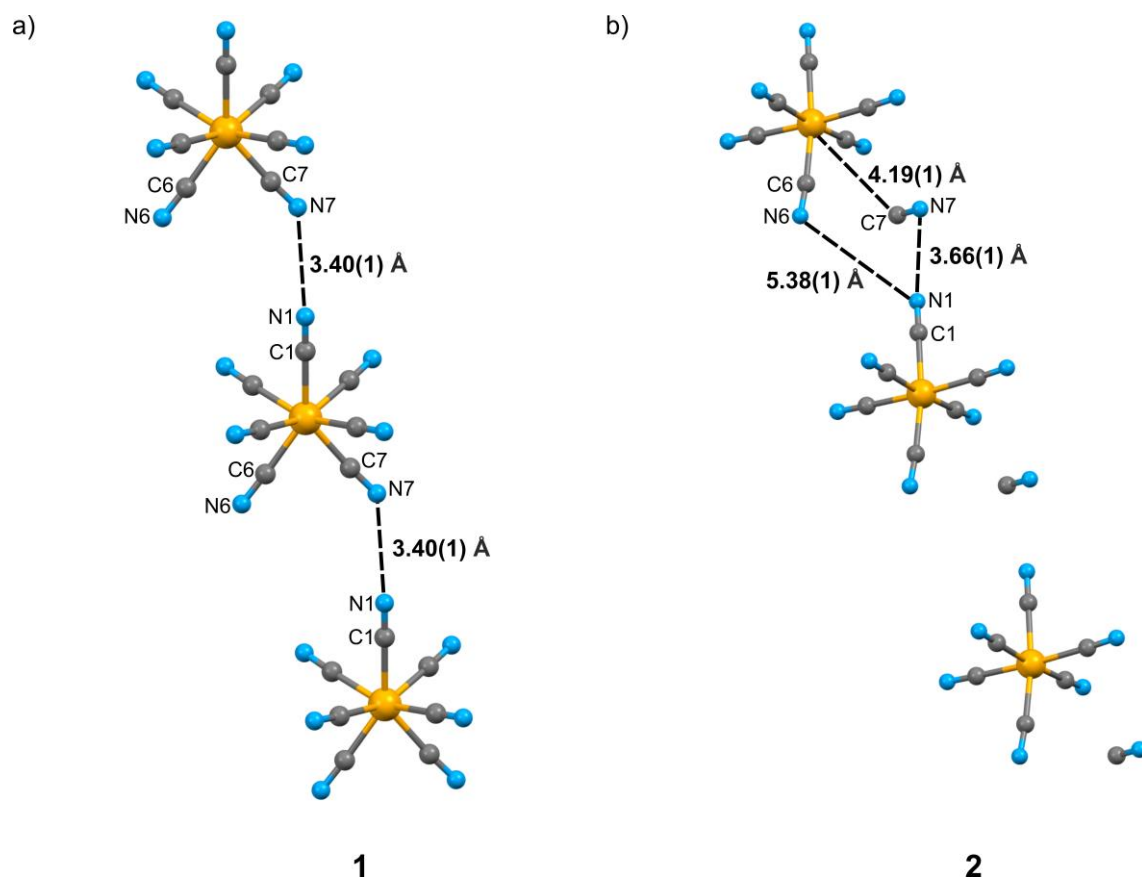
Figure S19. Fragments of the crystal structures at 30 K of **1** (a) and **2** (b) highlighting the supramolecular chain arrangement in **1**, and its disappeareance in **2** due to the cyanide dissociation.

Bulk magnetic properties of [K(crypt-222)]$_3$[Mo^{III}(CN)$_6$]·2CH$_3$CN (3)

The temperature dependence of magnetic susceptibility, χ, and its temperature product (χT) recorded for **3** in the 2-300 K range, were accurately reproduced by a S = 3/2 Curie law with g_{Mo} = 1.97(2) (Fig. S20).[20] Both the spin state of 3/2 and the g-factor slightly below 2.00 are in line with the expected $t_{2g}^3 e_g^0$ electronic configuration for Mo(III) in octahedral geometry. Accordingly, the magnetization value of 2.86 μ_B at 2 K and 7 T closely matches with 2.94 μ_B deduced from the S = 3/2 Brillouin function (Fig. S21).
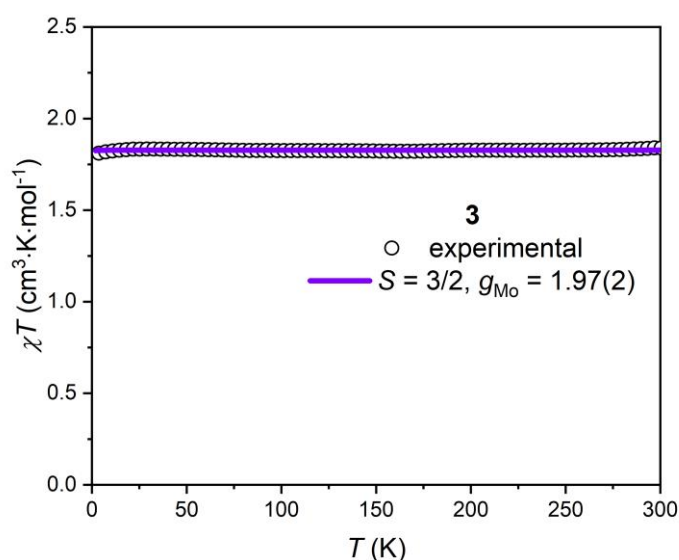

Figure S20. Temperature (T) dependence of the χT product at 0.1 T for **3** (where $\chi = M/H$ is the molar magnetic susceptibility normalized per complex). The solid purple line is the best fit of the data to a S = 3/2 Curie law (with g_{Mo} being the only ajustable parameter).
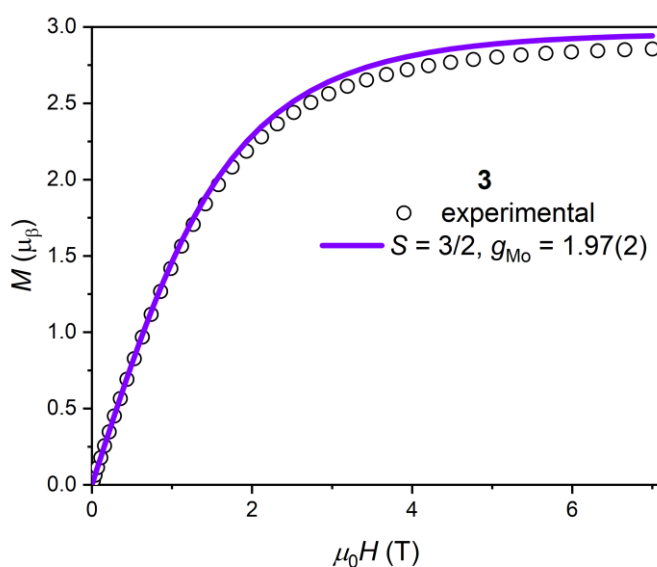

Figure S21. Field (H) dependence of the magnetization (M) for **3** at 2.0 K. The solid purple line is the simulated S = 3/2 Brillouin function with g_{Mo} =1.97.

Table S9. Stretched exponential decay fits of the relaxation data for **2** shown in Fig. 3e.[a]

T (K)	τ (s)	β	ΔχT / cm³·K·mol⁻¹	χT₀ / cm³·K·mol⁻¹	R²
132.5	10757(9)	1.339(2)	1.150(1)	0.4337(4)	0.99893
135	5305(5)	1.300(2)	1.181(1)	0.4321(2)	0.99899
137.5	3040(5)	1.328(4)	1.032(2)	0.4430(5)	0.99898
140	1688(4)	1.327(6)	1.074(2)	0.4399(7)	0.99858
142.5	939(3)	1.363(8)	1.02(3)	0.4410(7)	0.99818
145	491(2)	1.312(10)	0.945(3)	0.4389(6)	0.99820
147.5	260(2)	1.242(16)	0.781(5)	0.4412(9)	0.99710

[a]All data were fitted to the following equation: $\chi T = \Delta \chi T \cdot e^{-\left(\frac{t}{\tau}\right)^{\beta}} + \chi T_0$
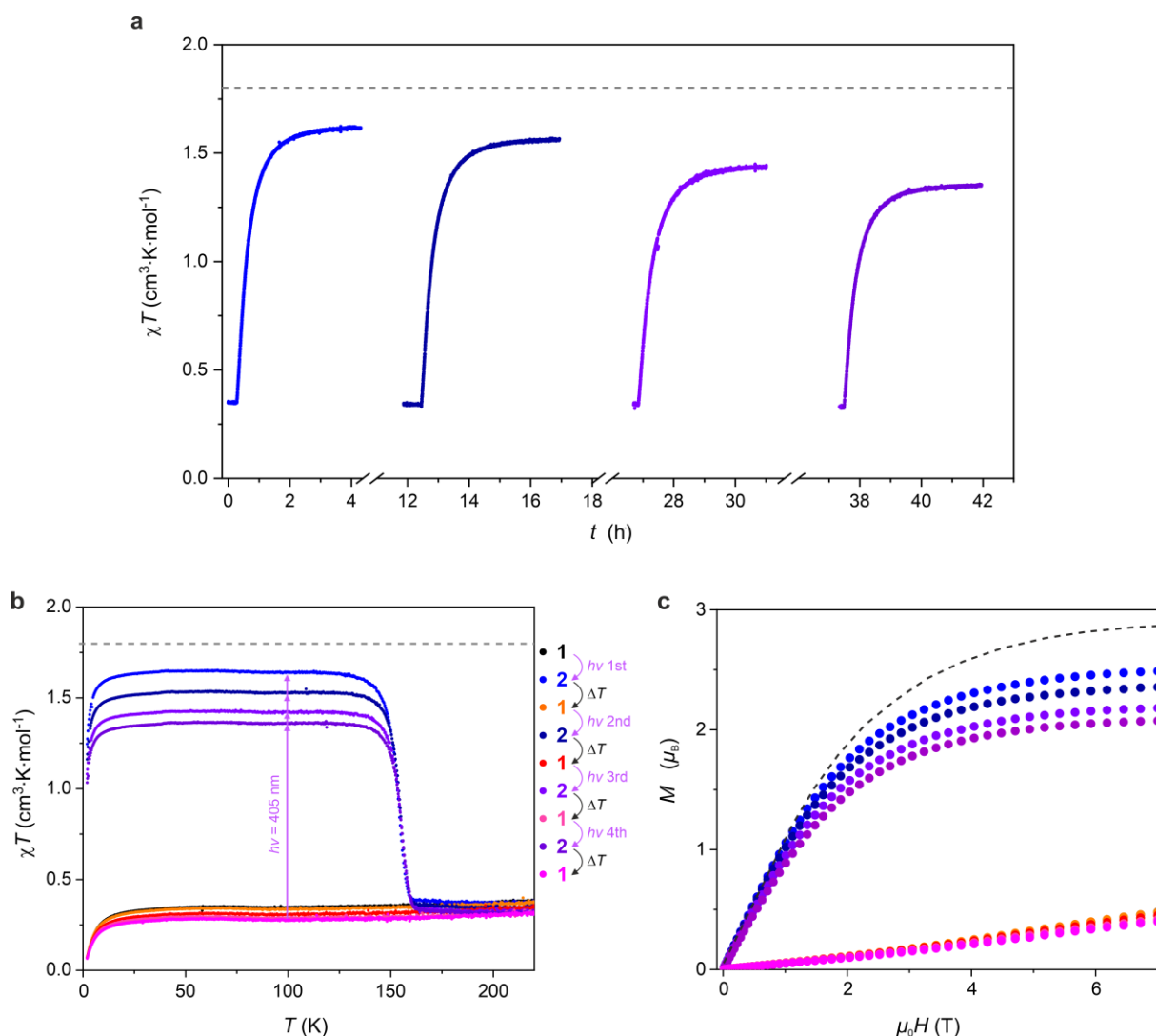
Figure S22. Photomagnetic studies of 1 after irradiation at 100 K. a, Time evolution of the χT product (at 0.1 T) of **1** during 4 consecutive cycles of 405 nm irradiation at 100 K, each followed by thermal relaxation at 220 K, confirming reversible photo-induced transformation **1→2**; **b**, Temperature dependence of the χT product at 0.1 T before (**1**) and after 405 nm irradiation (**2**) at 100 K in four consecutive irradiation and heating cycles as shown in Fig. S22a; **c**, Magnetization (*M*) versus magnetic field (*H*) plots for **1** (before irradiation) and **2** (after 405 nm irradiation) recorded at 2.0 K after four consecutive irradiation and heating cycles as shown in Fig. S22a. Dashed lines in all three plots indicate the χT (**a** and **b**) or M (**c**) values reached after the analogous irradiation experiments performed at 10 K presented in Figure 3.

References

1. Nakabayashi, K., Tomono, K., Tsunobuchi, Y., Kosaka, W. & Ohkoshi, S.-i. Tetrapotassium heptacyanidomolybdate(III) dihydrate. *Acta Crystallogr. E* **65**, i79-i80 (2009).

2. Alemany, P., Casanova, D., Alvarez, S., Dryzun, C. & Avnir, D. in Reviews in Computational Chemistry 289-352 (2017).

3. Beauvais, L.G. & Long, J.R. Cyanide-Limited Complexation of Molybdenum(III): Synthesis of Octahedral $[Mo(CN)_6]^{3-}$ and Cyano-Bridged $[Mo_2(CN)_{11}]$. *Journal of the American Chemical Society* **124**, 2110-2111 (2002).

4. Perdew, J.P., Burke, K. & Ernzerhof, M. Generalized Gradient Approximation Made Simple. *Phys. Rev. Lett.* **77**, 3865-3868 (1996).

5. Adamo, C. & Barone, V. Toward reliable density functional methods without adjustable parameters: The PBE0 model. *J. Chem. Phys.* **110**, 6158-6170 (1999).

6. Iikura, H., Tsuneda, T., Yanai, T. & Hirao, K. A long-range correction scheme for generalized-gradient-approximation exchange functionals. *J. Chem. Phys.* **115**, 3540-3544 (2001).

7. Lange, A.W., Rohrdanz, M.A. & Herbert, J.M. Charge-Transfer Excited States in a π-Stacked Adenine Dimer, As Predicted Using Long-Range-Corrected Time-Dependent Density Functional Theory. *The Journal of Physical Chemistry B* **112**, 7345-7345 (2008).

8. Weintraub, E., Henderson, T.M. & Scuseria, G.E. Long-Range-Corrected Hybrids Based on a New Model Exchange Hole. *Journal of Chemical Theory and Computation* **5**, 754-762 (2009).

9. Henderson, T.M., Izmaylov, A.F., Scuseria, G.E. & Savin, A. The importance of middle-range Hartree-Fock-type exchange for hybrid density functionals. *J. Chem. Phys.* **127** (2007).

10. Henderson, T.M., Izmaylov, A.F., Scuseria, G.E. & Savin, A. Assessment of a Middle-Range Hybrid Functional. *Journal of Chemical Theory and Computation* **4**, 1254-1262 (2008).

11. Vosko, S.H., Wilk, L. & Nusair, M. Accurate spin-dependent electron liquid correlation energies for local spin density calculations: a critical analysis. *Canadian Journal of Physics* **58**, 1200-1211 (1980).

12. Becke, A.D. Density-functional exchange-energy approximation with correct asymptotic behavior. *Physical Review A* **38**, 3098-3100 (1988).

13. Yanai, T., Tew, D.P. & Handy, N.C. A new hybrid exchange–correlation functional using the Coulomb-attenuating method (CAM-B3LYP). *Chem. Phys. Lett.* **393**, 51-57 (2004).

14. Grimme, S., Antony, J., Ehrlich, S. & Krieg, H. A consistent and accurate ab initio parametrization of density functional dispersion correction (DFT-D) for the 94 elements H-Pu. *J. Chem. Phys.* **132** (2010).

15. Grimme, S., Ehrlich, S. & Goerigk, L. Effect of the damping function in dispersion corrected density functional theory. *J. Comput. Chem.* **32**, 1456-1465 (2011).

16. Erba, A. et al. CRYSTAL23: A Program for Computational Solid State Physics and Chemistry. *Journal of Chemical Theory and Computation* **19**, 6891-6932 (2023).

17. Mulliken, R.S. Electronic Population Analysis on LCAO–MO Molecular Wave Functions. I. *J. Chem. Phys.* **23**, 1833-1840 (1955).

18. Bonner, J.C. & Fisher, M.E. Linear Magnetic Chains with Anisotropic Coupling. *Phys. Rev.* **135**, A640-A658 (1964).

19. Estes, W.E., Gavel, D.P., Hatfield, W.E. & Hodgson, D.J. Magnetic and structural characterization of dibromo- and dichlorobis(thiazole)copper(II). *Inorg. Chem.* **17**, 1415-1421 (1978).

20. Chilton, N.F., Anderson, R.P., Turner, L.D., Soncini, A. & Murray, K.S. PHI: A powerful new program for the analysis of anisotropic monomeric and exchange-coupled polynuclear d- and f-block complexes. *J. Comput. Chem.* **34**, 1164-1175 (2013).